Tunable metal hydroxide–organic frameworks for catalysing oxygen evolution

Shuai Yuan [1,2,8,10], Jiayu Peng [3,10], Bin Cai [1,2,9,10], Zhehao Huang [4], Angel T. Garcia-Esparza[5], Dimosthenis Sokaras[5], Yirui Zhang [6], Livia Giordano [1], Karthik Akkiraju[3], Yun Guang Zhu[1,6], René Hübner [7], Xiaodong Zou [4], Yuriy Román-Leshkov [2]✉ and Yang Shao-Horn [1,3,6]✉

The oxygen evolution reaction is central to making chemicals and energy carriers using electrons. Combining the great tunability of enzymatic systems with known oxide-based catalysts can create breakthrough opportunities to achieve both high activity and stability. Here we report a series of metal hydroxide–organic frameworks (MHOFs) synthesized by transforming layered hydroxides into two-dimensional sheets crosslinked using aromatic carboxylate linkers. MHOFs act as a tunable catalytic platform for the oxygen evolution reaction, where the π–π interactions between adjacent stacked linkers dictate stability, while the nature of transition metals in the hydroxides modulates catalytic activity. Substituting Ni-based MHOFs with acidic cations or electron-withdrawing linkers enhances oxygen evolution reaction activity by over three orders of magnitude per metal site, with Fe substitution achieving a mass activity of 80 A $g_{catalyst}^{-1}$ at 0.3 V overpotential for 20 h. Density functional theory calculations correlate the enhanced oxygen evolution reaction activity with the MHOF-based modulation of Ni redox and the optimized binding of oxygenated intermediates.

The oxygen evolution reaction (OER) is central to making carbon-free and carbon-neutral energy carriers such as hydrogen, hydrocarbons and ammonia using low-cost electrons from renewable energy[1], but the slow kinetics of the OER limit the power and energy efficiency of such devices[2]. Late transition metal oxides are known to exhibit high catalytic activity for the OER[2–4], which can be correlated with the binding strength of oxygenated intermediates[5] or intrinsic electronic structure features such as the e_g occupancy of transition metal cations[6] and oxygen p-band centre relative to the Fermi level[7]. Unfortunately, the most-active oxides based on Ni (ref. [3]) or Co (ref. [4]) have estimated turnover frequencies (TOFs) per metal site that are at least one order of magnitude lower than those of oxygen-evolving complexes in biological systems[8,9]. For example, the oxygen-evolving complex in photosystem II for water oxidation relies on an intricate manganese–calcium–oxo cluster $CaMn_4O_5$ (ref. [10]) that achieves unparalleled OER activity due to the unique electronic structure characteristics of Mn centres regulated by Ca^{2+} cations and carboxylate ligands[11]. Generally, metal substitution in metal–oxo clusters[12,13] has been shown to offer much greater tunability of electronic structure characteristics than that in metal oxides[14]. For instance, Ca^{2+} substitution of Mn^{4+} in synthetic $CaMn_3O_4$ clusters tunes the $Mn^{3+/4+}$ redox potential by ~1 V (refs. [12,13]), whereas negligible changes of ~0.02 V are typically observed after similar metal substitution in oxides[3,14]. Thus, immense opportunities exist to design hybrid organic–inorganic materials such as metal–organic frameworks (MOFs)[15,16] that combine the great tunability of enzymatic[11] or homogeneous systems[17] with the stability of oxides to break the current inherent limitations of traditional catalysts, including the large footprint[18] and poor stability[19].

MOFs are porous materials constructed by connecting inorganic building units (for example, metal clusters) with organic ligands using supramolecular chemistry[20], which provides a platform to design unique active-site environments for tuning electrocatalytic activity and selectivity[21]. Pioneer works have shown that Fe_2S_2 (ref. [22]), porphyrinic FeN_4 (ref. [23]) and CoN_4 (ref. [24]) centres embedded within the pores of MOFs can catalyse the electrochemical hydrogen evolution[22], oxygen reduction[23] and CO_2 reduction reactions[24], respectively. Recently, Tilley and coworkers have demonstrated OER activity using MOFs with Co_4O_4 clusters[25] analogous to those found in the oxygen-evolving complexes of enzymes. Moreover, the OER activity of MOFs based on Ni–OH and Co–OH layers featuring edge-sharing Ni- and Co-octahedral chains crosslinked through organic linkers[26] has been reported to rival that of the state-of-the-art catalysts[27]. Unfortunately, more recent studies have revealed that in alkaline electrolytes and at OER potentials, similar MOFs[28–30] decompose into Ni and Co hydroxides, which are well known to catalyse the OER[2,3]. Therefore, developing stable MOF catalysts in aqueous electrolytes and under oxidizing OER conditions is critical to fully leverage their unique capability to host highly tunable and active metal sites with ligand fields akin to those in enzymatic systems.

Here we developed a stable, active and highly tunable catalytic platform bridging transition metal oxides and MOFs by reacting layered hydroxides with aromatic carboxylate linkers to generate

MHOFs. We further established fundamental descriptors for the chemical stability, redox potential and OER activity of these MHOFs. Although traditional MOFs are typically connected by labile metal–ligand coordination bonds, these MHOFs are uniquely reinforced by strong π–π stacking interactions between linkers, resulting in stable MHOF lattices in alkaline OER conditions. Moreover, the number of electrochemically accessible active sites can be increased drastically by synthesizing MHOFs as ultra-thin nanosheets. Further optimization of Ni MHOF nanosheets via metal substitution resulted in a catalyst featuring a mass activity of 80 amperes per gram of the catalyst (A $g_{cat.}^{-1}$) and a TOF of 0.30 O_2 s^{-1} per electrochemically accessible metal site at 0.3 V overpotential in 0.1 M KOH for 20 h, exceeding the performance of commercial IrO_2 (Supplementary Table 1). The enhanced OER activity was attributed to the increased Ni redox potential and the optimized binding energy of oxygenated intermediates enabled by their unprecedented tunability.

Design and synthesis of stable MHOFs in alkaline solutions

Crystalline MHOFs were synthesized through solvothermal reactions between layered metal hydroxide precursors and aromatic organic linkers (Fig. 1a–c). A series of isostructural MHOFs were obtained from different metal ($M^{2+} = Mn^{2+}$, Co^{2+}, Ni^{2+}, Cu^{2+} and Zn^{2+}) and linker (L1, L2, L3, L4 and L4F) combinations, demonstrating the vast structural and compositional diversity attained using this method. While the powder X-ray diffraction patterns of $M_2(OH)_2(L4)$ were nearly identical (Supplementary Fig. 1), those with organic linkers of increasing length were shown to have the first diffraction peak shifted to lower angles (Fig. 1d), indicating larger interlayer spacing, which was further validated via Pawley refinement (Supplementary Fig. 2 and Supplementary Table 2). Moreover, we used continuous rotation electron diffraction to resolve the structure of $Ni_2(OH)_2(L4)$ from the reconstructed three-dimensional (3D) reciprocal lattice (Fig. 1e, Supplementary Fig. 3 and Supplementary Tables 3 and 4). High-resolution transmission electron microscopy (HR-TEM) images of $Ni_2(OH)_2(L4)$ (Fig. 1f and Supplementary Fig. 4) taken along the a axis match the atomic arrangements projected along the same direction (Fig. 1f inset), having lattice spacings for the (010) and (001) planes in agreement with those determined from powder X-ray diffraction (Supplementary Table 2). While it is known that hydroxides can be intercalated with anionic ligands (such as dicarboxylate[31] and disulfate[32]) to form lamellar compounds[33], the crystal structures of MHOFs are distinct from those of layered hydroxides (Supplementary Fig. 5 and Supplementary Note 1). In addition, in contrast to traditional MOFs with their high porosity and surface areas[20], MHOFs have relatively low Brunauer–Emmett–Teller surface areas, as indicated by N_2 adsorption measurements (Supplementary Fig. 6 and Supplementary Table 5).

Increasing the π–π interactions between organic linkers was shown to enhance the stability of MHOFs in alkaline solutions (Fig. 1g and Supplementary Figs. 7 and 8), a result that stands apart from conventional MOFs composed of M^{2+} metals linked with carboxylates that readily decompose in water[34]. While $Ni_2(OH)_2(L1)$ showed the lowest stability, leached out a majority of the organic linkers, lost crystallinity and generated amorphous $Ni(OH)_2$ after 6 h in KOH, $Ni_2(OH)_2(L4)$ exhibited the highest stability, where no substantial changes in the composition and crystallinity were detected after 24 h. Both the leaching rate of linkers and the steady-state molar concentration of dissolved linkers on a logarithmic scale were found to decrease linearly with increasing π–π stacking energy in MHOFs (Fig. 1h and Supplementary Figs. 9 and 10), which could be attributed to the increased kinetic barrier and/or decreased thermodynamic driving force for the leaching of these linkers. Notably, the stability of $Ni_2(OH)_2(L4)$ and $Ni_2(OH)_2(L4F)$ in alkaline solutions is among the highest reported for MOFs, comparable to that

of MOFs based on Ni–azolate, which are known for their record stability[34]. Thus, $Ni_2(OH)_2(L4)$ and $Ni_2(OH)_2(L4F)$ were selected for further studies.

Synthesis and electrochemical measurement of MHOF nanosheets

Synthesizing Ni MHOFs in a nanosheet architecture can increase the number of electrochemically active metal sites available for (electro)catalysis. By reacting $NiCl_2 \cdot 6H_2O$ (instead of $Ni(OH)_2$) with the respective linker, we were able to grow MHOFs in the bc plane (that is, against the Ni–OH layer direction) as nanosheets (Fig. 2a). Powder X-ray diffraction patterns of $Ni_2(OH)_2(L4)$ nanosheets showed the absence of ($h00$) reflections, while the ($0k0$) and ($00l$) diffraction peaks remained sharp, indicating reduced dimensions along the a axis and unaltered lattice structure within the bc plane (Supplementary Fig. 11). Scanning electron microscopy (Fig. 2b and Supplementary Fig. 12) and TEM (Fig. 2c and Supplementary Fig. 13) showed $Ni_2(OH)_2(L4)$ nanosheets with a regular rectangular shape, and the (100) surface termination of $Ni_2(OH)_2(L4)$ nanosheets was further verified by HR-TEM (Fig. 2c) and electron diffraction (Supplementary Fig. 14). Lattice fringe spacings of 0.61 nm and 1.60 nm shown by HR-TEM are consistent with the interplanar spacings along the b and c axes of the structure of $Ni_2(OH)_2(L4)$ computed from powder X-ray diffraction refinement ($b = 0.62$ nm and $c = 1.57$ nm, respectively; Supplementary Table 2). A thickness of ~4.2 nm was found for $Ni_2(OH)_2(L4)$ nanosheets using atomic force microscopy (Supplementary Fig. 15), corresponding to approximately 12 unit cells. Notably, $Ni_2(OH)_2(L4)$ nanosheets were found to have a 15 times larger electrochemically active surface area than bulk $Ni_2(OH)_2(L4)$ per unit weight (Supplementary Fig. 16), quantified by integrating the charge of the redox peaks at 1.38 V versus the reversible hydrogen electrode scale (V_{RHE}) measured using cyclic voltammetry (CV) in 0.1 M KOH. This result is consistent with a higher weight loss below 300 °C for $Ni_2(OH)_2(L4)$ nanosheets compared with bulk samples in thermogravimetric analysis, presumably attributable to more water removal from surface Ni sites (Supplementary Fig. 17). Moreover, a similar synthetic strategy was used to fabricate $Ni_2(OH)_2(L1)$, $Ni_2(OH)_2(L2)$, $Ni_2(OH)_2(L3)$ and $Ni_2(OH)_2(L4F)$ nanosheets with characterization results (Fig. 2d and Supplementary Figs. 18 and 19) comparable to those of $Ni_2(OH)_2(L4)$, highlighting the universality of this synthetic approach for MHOF nanosheets.

Tuning the nickel redox of MHOFs by metal substitution

We substituted the Ni^{2+} cations in $Ni_2(OH)_2(L4)$ nanosheets with comparable percentages of electron-withdrawing heterometal substituents (La^{3+}, Zn^{2+}, Y^{3+}, Al^{3+}, Sc^{3+} and Fe^{3+}, between ~12.5 and ~17.9 at.%; Supplementary Table 6). Elemental mapping based on energy-dispersive X-ray analysis, conducted by scanning electron microscopy and TEM, showed homogeneous distribution of substituents in these nanosheets (Supplementary Figs. 20 and 21). No pronounced changes were observed in the powder X-ray diffraction patterns and unit cell dimensions (quantified via Pawley refinement) of $M/Ni_2(OH)_2(L4)$ with different heterometal substituents (Supplementary Figs. 22–24 and Supplementary Table 7). Moreover, X-ray photoelectron spectroscopy (XPS; Supplementary Fig. 25) and Ni K-edge X-ray absorption near-edge structure (Supplementary Fig. 26a,b) analyses of $M/Ni_2(OH)_2(L4)$ showed negligible changes in the surface and bulk oxidation state of Ni^{2+} introduced by metal substitution, respectively. The negligible shift of Ni 2p XPS peaks for $M/Ni_2(OH)_2(L4)$, falling within the experimental uncertainty of laboratory XPS (~0.1 eV)[35], can be attributed to the low substitution levels in $M/Ni_2(OH)_2(L4)$ (Supplementary Note 2). The X-ray absorption near-edge structure of $M/Ni_2(OH)_2(L4)$ indicated no notable changes in the Ni K-edge (Supplementary Fig. 26a,b),
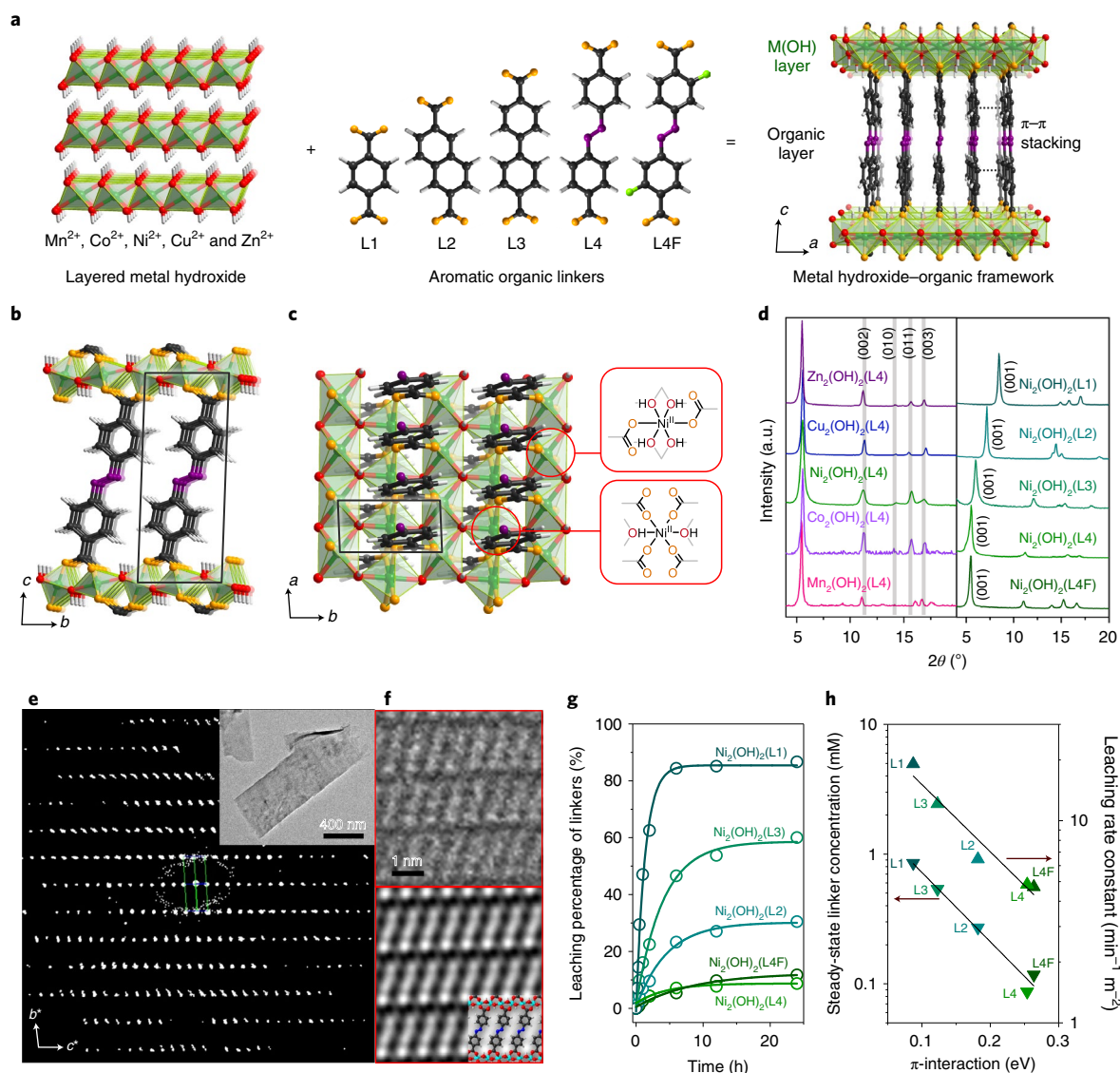
Fig. 1 | Structural design and stability optimization of MHOFs. a, Schematic representation of the MHOF assembly process, illustrating metal hydroxide layers comprising edge-sharing metal-octahedral chains crosslinked with neighbouring chains via organic linkers (L1, terephthalate; L2, 2,6-naphthalene dicarboxylate; L3, 4,4′-biphenyl dicarboxylate; L4, azobenzene-4,4′-dicarboxylate and L4F, 2,2′-difluoroazobenzene-4,4′-dicarboxylate). **b**, The structure of $Ni_2(OH)_2(L4)$ viewed along the *a* direction. **c**, The structure of $Ni_2(OH)_2(L4)$ viewed along the *c* direction. Insets: the coordination environments of two crystallographically independent Ni ions. Unit cell axes are indicated by the black arrows. Colour scheme: Ni, green; O from μ_3-OH, red; O from μ_3-COO, orange; C, black; N, purple; F, light green; H, white. Black boxes in **b** and **c** indicate a unit cell of MHOF. **d**, Powder X-ray diffraction of MHOFs with different linkers (L1, L2, L3, L4 and L4F) and metals ($M^{2+} = Mn^{2+}$, Co^{2+}, Ni^{2+}, Cu^{2+} and Zn^{2+}), where 2θ is the angle between the transmitted and reflected X-rays. **e**, Reconstructed 3D reciprocal lattice of $Ni_2(OH)_2(L4)$ based on continuous rotation electron diffraction data along the *a** direction. Inset: the MHOF crystal for continuous rotation electron diffraction data collection. **f**, HR-TEM image along the *a* direction (top) and the symmetry-imposed and lattice-averaged HR-TEM image along with the crystal structure overlaid on the image (bottom). **g**, Leaching percentage of linkers monitored by UV–vis spectroscopy during stability tests in 0.1 M KOH at room temperature. Linker leaching percentage is defined as the number of linkers in the solution divided by the number of linkers in MHOFs before the stability test, where the concentrations of L1, L2, L3, L4 and L4F were calculated from the UV–vis absorbance at 240 nm, 284 nm, 278 nm, 331 nm and 332 nm, respectively (Supplementary Fig. 7). **h**, Dependence of steady-state linker concentration after 24 h and linker leaching rate constant (Supplementary Fig. 10) normalized by the Brunauer–Emmett–Teller surface area of $Ni_2(OH)_2(L)$ (L = L1, L2, L3, L4 and L4F) before leaching (time, $t = 0$) on the π-stacking energy of different organic linkers (Supplementary Fig. 9).

supporting the idea that the first-shell coordination and oxidation state of Ni were mostly unchanged after metal substitution. The Fe K-edge X-ray absorption near-edge structure of $Fe/Ni_2(OH)_2(L4)$ further confirmed the existence of Fe^{3+} in octahedral coordination (Supplementary Fig. 26c), in agreement with the partial replacement of Ni^{2+} cations by Fe^{3+} ions in NiO_6 octahedra. This observation is consistent with the diffuse reflectance infrared Fourier transform

spectra of $Fe/Ni_2(OH)_2(L4)$ with a reduced O–H stretching peak at ~3,600 cm^{-1} (Supplementary Fig. 27a), expected from the removal of protons from –OH groups in MHOFs upon Fe^{3+} substitution (Supplementary Fig. 27b). Thus, Fe-substituted $(Ni^{2+})_2(OH)_2(L4)$ can be expressed as $(Fe^{3+})_{0.2}(Ni^{2+})_{1.8}(OH)_{1.8}(O)_{0.2}(L4)$, having a charge compensation different from that in Fe-substituted Ni hydroxides, where the charge is compensated by the interlayer
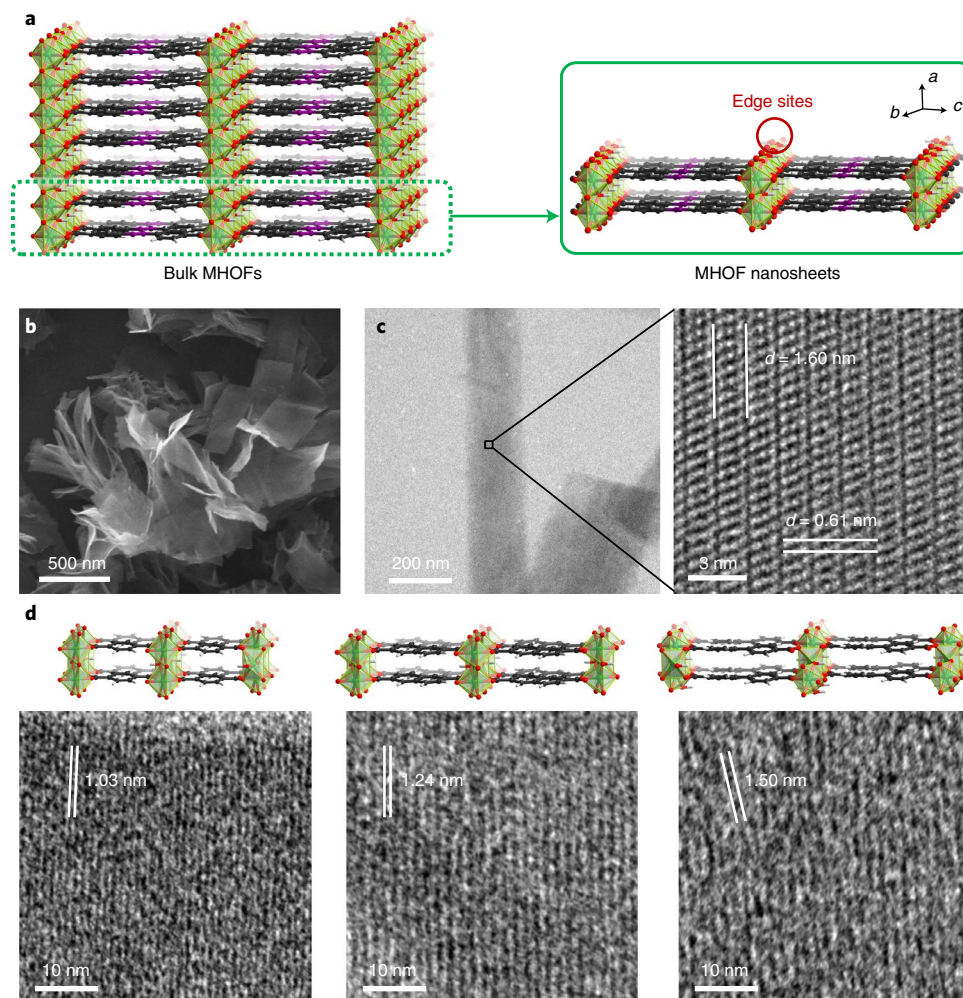
Fig. 2 | Synthesis of MHOF nanosheets. a, Schematic representation of the growth direction of MHOF nanosheets. **b,c**, Scanning electron microscopy (**b**) and TEM images (**c**) of $Ni_2(OH)_2(L4)$ nanosheets, showing the two-dimensional morphology and lattice fringes. **d**, TEM images and corresponding structures of $Ni_2(OH)_2(L1)$ (left), $Ni_2(OH)_2(L2)$ (middle) and $Ni_2(OH)_2(L3)$ (right) nanosheets. The axis lengths (from powder X-ray diffraction refinement) match the lattice fringe spacings (*d*, from HR-TEM), confirming the growth of nanosheets within the *bc* plane. The *c*-axis lengths are 1.06 nm, 1.23 nm and 1.45 nm for $Ni_2(OH)_2(L1)$, $Ni_2(OH)_2(L2)$ and $Ni_2(OH)_2(L3)$, respectively, in agreement with the lattice fringe spacings shown in **d**. (Supplementary Table 2). Colour scheme: Ni, green; O, red; C, black; N, purple; H, white.

intercalation of anions (for example, CO_3^{2-}, NO_3^-, SO_4^{2-} and Cl^- (ref. [36]); Supplementary Fig. 27c).

The redox potential of Ni centres at ~1.38 V_{RHE} was found to shift positively with more acidic (that is, more electron-withdrawing) substituents in $M/Ni_2(OH)_2(L4)$ (M = La^{3+}, Zn^{2+}, Y^{3+}, Al^{3+}, Sc^{3+} and Fe^{3+}; Fig. 3a,b), as described by the lowered pK_a of corresponding hydrated metal cations (that is, $[M(H_2O)_m]^{n+})^{37}$. The Ni redox in $M/Ni_2(OH)_2(L4)$ was evaluated using samples with similar substitution levels (12.5–17.9 at.%) since the substitution level can also influence the Ni redox potential (Supplementary Fig. 28 and Supplementary Note 3). Moreover, the dependence of the Ni redox potential of $M/Ni_2(OH)_2(L4)$ on the acidity of substituents is much stronger than that of structural parameters such as the ionic radii of heterometals (Supplementary Fig. 29 and Supplementary Note 3). This result is consistent with the negligible changes of Ni–O and Ni⋯Ni atomic distances in substituted $Ni_2(OH)_2(L4)$ nanosheets (Fig. 3c and Supplementary Fig. 30), as shown by the Ni K-edge extended X-ray absorption fine structure of $M/Ni_2(OH)_2(L4)$ (Supplementary Figs. 31–34 and Supplementary Tables 8–15). Therefore, the change in the Ni redox potential of $M/Ni_2(OH)_2(L4)$ (Fig. 3a) can be attributed mainly to a systematic inductive effect on

the Ni–O bonds in substituted MHOFs introduced by the different electron-withdrawing nature of metal substituents.

Remarkably, the shift in the Ni redox of MHOFs upon metal substitution (up to ~0.1 V; Fig. 3b) was five times greater than that of substituted Ni hydroxides (~0.02 V) with similar substitution levels (~10 at.%)[14]; 12.5 at.% Fe-substituted $Ni_2(OH)_2(L4)$ featured a Ni redox potential at 1.45 V_{RHE}, considerably higher than that of Fe-substituted Ni hydroxides (1.37 V_{RHE}, 10 at.% Fe (ref. [14]); Fig. 3b). Taken together, these results show that the redox of metal centres in MHOFs can be tuned much more effectively relative to their metal oxide and hydroxide counterparts.

Tuning the OER activity of MHOFs by metal substitution
Incorporating increasingly electron-withdrawing heterometal substituents in $M/Ni_2(OH)_2(L4)$ nanosheets markedly enhanced their OER activity. Galvanostatic measurements of $M/Ni_2(OH)_2(L4)$ nanosheets showed that the steady-state OER overpotentials were reduced linearly with more acidic metals and more positively shifted pre-OER Ni redox (in the order of $La^{3+} < Zn^{2+} < Y^{3+} < Al^{3+} < Sc^{3+} < Fe^{3+}$; Fig. 4a,b), in agreement with reduced OER potentials in CV measurements (Supplementary Fig. 35). This observation
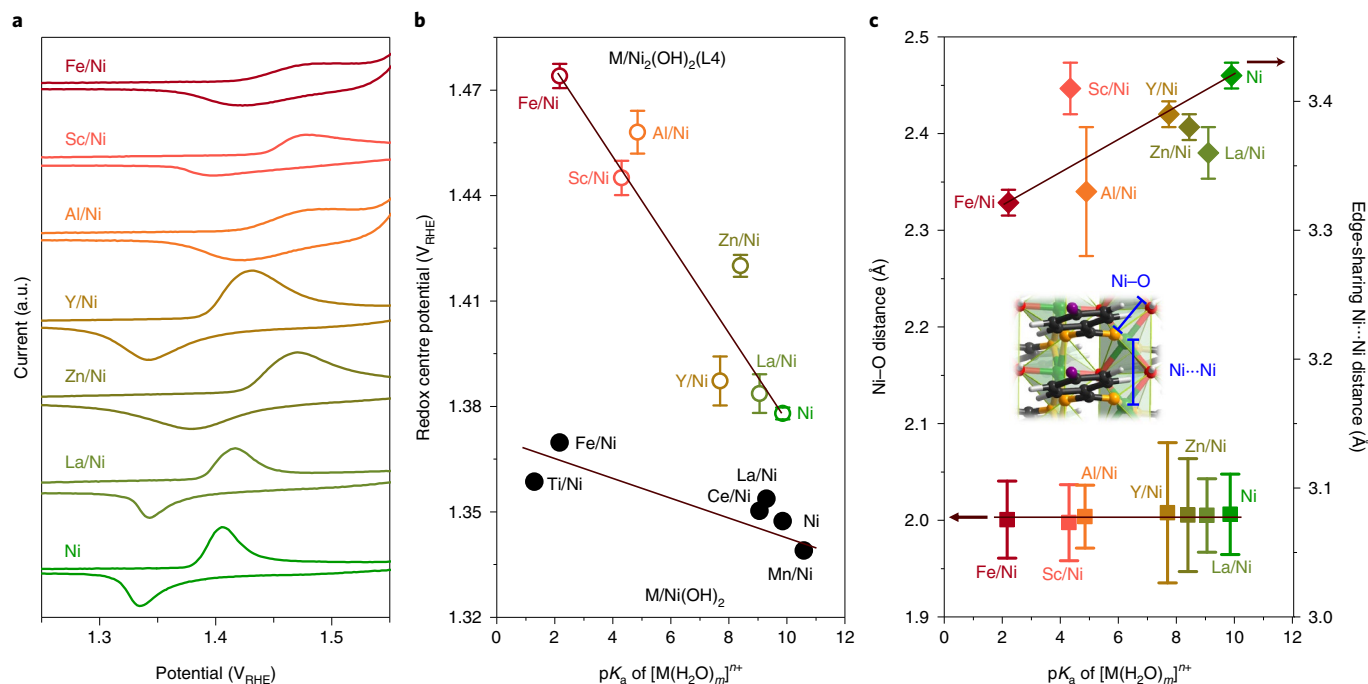
**Fig. 3 | Tuning the electronic structure of M/Ni$_2$(OH)$_2$(L4) nanosheets. a**, CV measurements of M/Ni$_2$(OH)$_2$(L4) nanosheets substituted with heterometals showing shifted Ni redox peaks. CV measurements were conducted in Ar-saturated 0.1 M KOH at 10 mV s^{-1} using electrodes composed of 125 μg$_{cat.}$ cm$_{geo.}^{-2}$ and 20 μg$_{Nafion}$ cm$_{geo.}^{-2}$. Heterometal substitution levels were 17.9 at.% for La, 17.0 at.% for Zn, 17.6 at.% for Y, 15.9 at.% for Al, 16.7 at.% for Sc and 12.5 at.% for Fe (measured by inductively coupled plasma optical emission spectroscopy). **b**, Redox centre of Ni determined from CV as a function of the pK_a of hydrated metal ions [M(H$_2$O)$_m$]$^{n+}$ in substituted Ni(OH)$_2$ (solid black circles) and Ni$_2$(OH)$_2$(L4) nanosheets (empty circles). Redox centres of metal-substituted Ni(OH)$_2$ (ref. [14]) and pK_a values[37] were taken from previous works. Error bars represent the standard deviations of at least three independent measurements. **c**, Ni–O and edge-sharing Ni⋯Ni distances in M/Ni$_2$(OH)$_2$(L4) obtained from Ni K-edge extended X-ray absorption fine structure fitting as a function of the pK_a of hydrated metal ions [M(H$_2$O)$_m$]$^{n+}$. Inset: schematics of Ni–O and Ni⋯Ni distances. Colour scheme: Ni, green; O from μ$_3$-OH, red; O from μ$_3$-COO, orange; C, black; N, purple; H, white. Error bars represent the uncertainty of parameters fitted with extended X-ray absorption fine structure.

is consistent with the functionalization of the L4 linkers with electron-withdrawing fluorine groups leading to a higher Ni redox potential and potentially increased activity (Supplementary Fig. 36 and Supplementary Note 3). We thus postulate that the enhanced OER activity can be attributed to more electron-deficient Ni centres introduced by more acidic substituents via the inductive effect.

To elucidate the role of the inductive effect, we performed density functional theory (DFT) calculations of the pre-OER metal redox (Supplementary Tables 16 and 17) and OER energetics (Supplementary Table 18) on the (100) surface of Ni$_2$(OH)$_2$(L4) and Fe/Ni$_2$(OH)$_2$(L4). According to the surface Pourbaix diagrams (Supplementary Fig. 37), the surface Ni sites in Ni MHOFs are covered by adsorbed H$_2$O species (H$_2$O$_{ad}$) at open circuit, consistent with the observation that such surface Ni ions are Ni^{2+} (Supplementary Fig. 38 and Supplementary Note 4). This result agrees with the observation that Ni MHOF nanosheets, with a higher portion of surface Ni than bulk Ni MHOFs, had more water removal from surface Ni^{2+} sites, as indicated by thermogravimetric analysis (Supplementary Fig. 17). Moreover, the Ni redox at 1.38 V$_{RHE}$ for Ni$_2$(OH)$_2$(L4) (Fig. 3a) can be attributed to Ni^{2+} oxidation coupled with the deprotonation of Ni–H$_2$O into Ni–OH (for example, Ni^{2+}–H$_2$O + OH$^-$ → Ni^{3+}–OH + H$_2$O + e$^-$; Fig. 4c), and the potential for Ni^{2+} oxidation in Fe/Ni MHOFs is higher than that in Ni MHOFs (Supplementary Fig. 38). These observations can be rationalized by the inductive effect. Specifically, Fe^{3+}, with higher acidity than Ni^{2+}, can pull electrons from neighbouring Ni–O bonds, lowering the electron energy associated with the oxidation of Ni^{2+} and shifting the corresponding Ni redox positively. Furthermore, based

on the proton-coupled electron transfer (PCET) OER mechanism (Fig. 4c)[4,9,27], Ni centres (*Ni–Ni–Ni, with * indicating the surface metal sites) in Ni$_2$(OH)$_2$(L4) were found to have a large barrier from OH$_{ad}$ to O$_{ad}$ (0.56 eV at 1.6 V$_{RHE}$; Fig. 4d). However, this barrier is reduced substantially on the two Ni sites in Fe/Ni$_2$(OH)$_2$(L4) (Fig. 4d and Supplementary Fig. 39), where one Ni site (*Ni–Ni–Fe) has a barrier of 0.23 eV at 1.6 V$_{RHE}$ for rate-limiting OH$_{ad}$ deprotonation, and the other (*Ni–Fe–Ni) has OH$_{ad}$ adsorption as the rate-determining step (RDS) with a barrier of 0.3 eV at 1.6 V$_{RHE}$. Such a reduced barrier is consistent with having highly acidic Fe^{3+} cations in Fe/Ni$_2$(OH)$_2$(L4), as Fe^{3+} destabilizes OH$_{ad}$ on surface Ni sites, leading to a higher potential for the deprotonation of H$_2$O$_{ad}$ to OH$_{ad}$ and a reduced barrier for further OH$_{ad}$ deprotonation (Fig. 4d).

These DFT results have examined the traditional PCET OER pathway involving only concerted proton–electron transfer steps of a single oxygenated species on a single metal site. While the surface Fe sites (*Fe–Ni–Ni) in Fe/Ni$_2$(OH)$_2$(L4) were found to have a lower barrier (0.11 eV for the RDS, O–O coupling, at 1.6 V$_{RHE}$) than Ni sites (for example, 0.23 V for *Ni–Ni–Fe at 1.6 V$_{RHE}$; Fig. 4d), further theoretical Tafel slope analysis based on the coverage of OER intermediates before the RDS[38,39] in the PCET energetics favours Ni sites as the active sites (Supplementary Fig. 40, Supplementary Table 19 and Supplementary Note 5). Specifically, for *Fe–Ni–Ni sites (with O–O bond formation as the RDS), as all the steps before the RDS are energetically downhill at OER potentials (for example, 1.5–1.9 V$_{RHE}$), such Fe sites are dominantly covered by O$_{ad}$ in this potential range and have a Tafel slope of 120 mV per decade (dec; Supplementary Fig. 40d). Similarly, *Ni–Fe–Ni centres (with OH$_{ad}$ adsorption as the
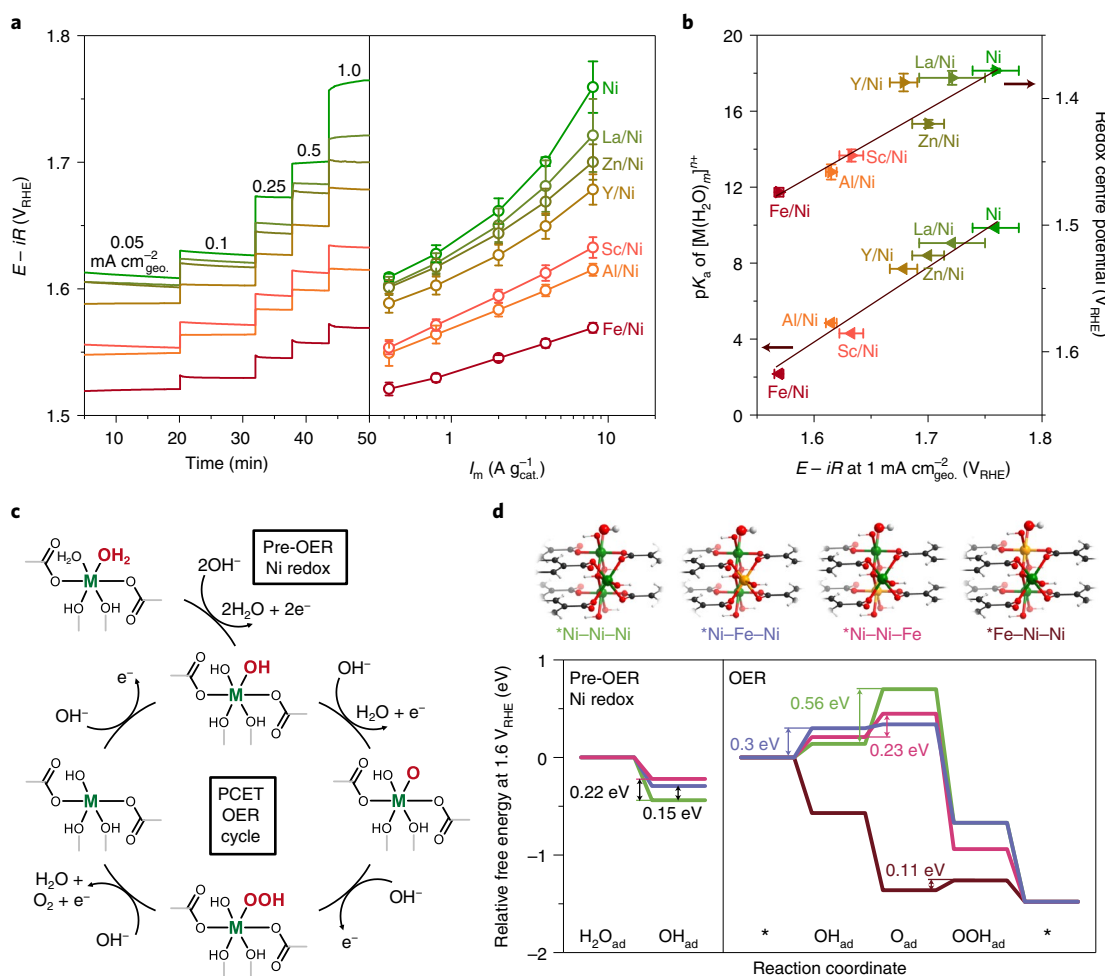
Fig. 4 | Tuning the OER activity of M/Ni₂(OH)₂(L4) nanosheets. a, Galvanostatic measurements and Tafel plots of OER activity for metal-substituted Ni$_2$(OH)$_2$(L4) nanosheets using electrodes composed of 125 µg$_{cat.}$ cm$^{-2}_{geo.}$ and 20 µg$_{Nafion}$ cm$^{-2}_{geo.}$ in O$_2$-saturated 0.1 M KOH at 1,600 r.p.m. after iR correction, where E is the electrode potential, and I_m is the mass-normalized current density. Heterometal substitution levels were 17.9 at.% for La, 17.0 at.% for Zn, 17.6 at.% for Y, 15.9 at.% for Al, 16.7 at.% for Sc and 12.5 at.% for Fe (based on inductively coupled plasma optical emission spectroscopy measurements). **b**, OER steady-state potential (at 1 mA cm$^{-2}_{geo.}$, with iR correction) as a function of the pK_a of hydrated metal cations [M(H$_2$O)$_m$]$^{n+}$ (obtained from previous work)[37] in metal-substituted Ni$_2$(OH)$_2$(L4) nanosheets and their pre-OER Ni redox centres (Fig. 3b). Error bars in **a** and **b** represent the standard deviations of at least three independent measurements. **c**, Proposed PCET OER cycle and the corresponding pre-OER Ni redox step for Ni and Fe/Ni MHOFs. **d**, DFT free energy diagrams of pre-OER Ni redox and PCET OER steps for the (100) surface of Ni$_2$(OH)$_2$(L4) and Fe/Ni$_2$(OH)$_2$(L4) at 1.6 V$_{RHE}$. Ni redox energetics are plotted based on the driving force of pure Ni redox transitions for Ni$_2$(OH)$_2$(L4) and Fe/Ni$_2$(OH)$_2$(L4) (Supplementary Fig. 38). Energetic barriers of the RDS for all possible surface metal sites (highlighted with * and shown by surface models) are labelled in the free energy diagram. Colour scheme: Ni, green; Fe, yellow; O, red; C, black; H, white.

RDS) are predicted to be covered by empty sites and show a Tafel slope of 120 mV dec^{-1} at OER potentials (Supplementary Fig. 40b). By contrast, *Ni–Ni–Fe sites, with OH$_{ad}$ deprotonation as the RDS and an electrochemical pre-equilibrium step (that is, OH$_{ad}$ adsorption on empty sites) before the RDS, are predicted to be covered by empty sites with a Tafel slope of 40 mV dec^{-1} below 1.7 V$_{RHE}$, while above 1.9 V$_{RHE}$, these *Ni–Ni–Fe sites are dominantly covered by OH$_{ad}$ with a Tafel slope of 120 mV dec^{-1}. Thus, compared with the other metal centres, the predicted Tafel slope of *Ni–Ni–Fe centres below 1.7 V$_{RHE}$ is in better agreement with the measured Tafel slopes of Fe/Ni MHOFs (between 35 mV dec^{-1} and 40 mV dec^{-1} at 1.52–1.56 V$_{RHE}$; Fig. 4a and Supplementary Table 20). Nevertheless, in light of the different schools of thought[40–44] on the OER active centres in Fe/Ni hydroxides (Supplementary Note 6), more complex pathways (for example, involving the joint contribution of surface Fe and Ni sites)[42–44] need to be explored in future studies to fully understand the active sites in Fe/Ni MHOFs. This need is

supported by the pH-dependent Ni redox (−17 mV$_{RHE}$ per pH unit) and OER potential (−19 mV$_{RHE}$ per pH unit) of Fe/Ni$_2$(OH)$_2$(L4) on the reversible hydrogen electrode scale (Supplementary Fig. 41), which cannot be explained by the PCET mechanism (Fig. 4c). Such pH dependence suggests Ni redox and OER steps involving the non-concerted transfer of protons and electrons[45–47], resulting in more complex intermediates and pathways beyond the conventional PCET scheme (Supplementary Fig. 42 and Supplementary Note 7). Future work combining ab initio calculations and in situ spectroscopies can provide more mechanistic insights into the OER on Fe/Ni MHOFs.

Mixing Fe/Ni$_2$(OH)$_2$(L4) nanosheets with carbon markedly enhanced the percentage of electrochemically accessible Ni sites (from 0.1% to 16%; Supplementary Fig. 43), giving rise to an increase in mass activity by ~100 times to 80 A g$^{-1}_{cat.}$ at an overpotential of 0.3 V (Fig. 5a), considerably higher than that of commercial IrO$_2$ catalysts measured in this work and reported previously[48].
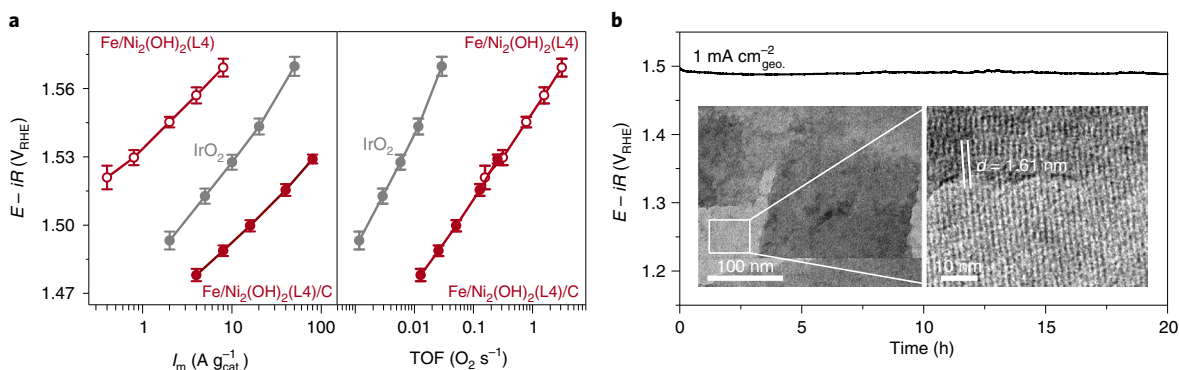
Fig. 5 | Activity optimization of Fe/Ni$_2$(OH)$_2$(L4) nanosheets. a, Tafel plots of the OER mass activity and TOF of Fe/Ni$_2$(OH)$_2$(L4) and Fe/Ni$_2$(OH)$_2$(L4)/C nanosheets, as well as commercial IrO$_2$, quantified through galvanostatic measurements. TOFs were calculated by dividing the oxygen flux (O$_2$ s^{-1}) converted from the OER current (assuming 100% Faradaic efficiency) by the number of electrochemically accessible metals (Ni + Fe; Supplementary Table 1). Error bars represent the standard deviations of at least three independent measurements. **b,** Long-term galvanostatic test of Fe/Ni$_2$(OH)$_2$(L4)/C at 1 mA cm$^{-2}_{geo.}$. Inset: the TEM images of Fe/Ni$_2$(OH)$_2$(L4)/C after the OER. All galvanostatic measurements were performed in O$_2$-saturated 0.1 M KOH at 1,600 r.p.m. after *iR* correction, where the electrodes of Fe/Ni$_2$(OH)$_2$(L4) consisted of 125 µg$_{cat.}$ cm$^{-2}_{geo.}$ and 20 µg$_{Nafion}$ cm$^{-2}_{geo.}$, and an additional 25 µg cm$^{-2}_{geo.}$ of acid-treated acetylene carbon black was used for Fe/Ni$_2$(OH)$_2$(L4)/C.

On the other hand, the intrinsic activity of Fe/Ni$_2$(OH)$_2$(L4) nanosheets was unchanged with carbon addition (Fig. 5a). Fe/Ni$_2$(OH)$_2$(L4)/C was found to have a high specific activity (with oxygen fluxes or TOFs of 0.30 O$_2$ s^{-1} per electrochemically accessible metal site as an upper bound, and 0.05 O$_2$ s^{-1} per total metal site as a lower bound, at 0.3 V overpotential), comparing favourably to state-of-the-art oxide catalysts[46,49,50] (Supplementary Table 1 and Supplementary Note 8). Carbon-supported Fe/Ni$_2$(OH)$_2$(L4) nanosheets were shown to provide steady-state current densities up to 50 milliamperes per geometric square centimetre (mA cm$^{-2}_{geo.}$) for tens of hours in 0.1 M KOH (Supplementary Fig. 44), and TEM revealed no pronounced changes in the morphology and crystallinity after the OER at 1 mA cm$^{-2}_{geo.}$ for 20 h (Fig. 5b), highlighting the electrochemical stability of Fe/Ni$_2$(OH)$_2$(L4)/C under alkaline OER conditions.

In conclusion, we have developed a series of MHOFs combining the advantages of molecular catalysts (with highly tunable electronic structures) and metal oxides (with high stability under alkaline OER conditions). The stability of MHOFs is governed by π-stacking interactions between linkers connecting adjacent hydroxide layers, with Ni$_2$(OH)$_2$(L4) featuring the highest stability in 0.1 M KOH. Reducing the dimensions of bulk MHOFs into nanosheets exposes more surface metal sites, resulting in a greater amount of electrochemically active surface areas. Substituting more acidic metal cations into Ni MHOFs was found to increase the redox potential of Ni as well as the OER activity, which can be attributed to electrons withdrawing from Ni via the inductive effect, leading to Fe/Ni$_2$(OH)$_2$(L4)/C with activity rivalling those of state-of-the-art OER catalysts. This work represents a step forward towards designing active metal centres with ligand fields akin to those in enzymatic systems. The compositional and structural flexibility of MHOFs offers immense opportunities to engineer tunable redox properties and catalytic activity for processes including the OER and beyond.

Online content

Any methods, additional references, Nature Research reporting summaries, source data, extended data, supplementary information, acknowledgements, peer review information; details of author contributions and competing interests; and statements of data and code availability are available at https://doi.org/10.1038/s41563-022-01199-0.

References

1. Gray, H. B. Powering the planet with solar fuel. *Nat. Chem.* **1**, 7 (2009).
2. Wei, C. et al. Recommended practices and benchmark activity for hydrogen and oxygen electrocatalysis in water splitting and fuel cells. *Adv. Mater.* **31**, 1806296 (2019).
3. Enman, L. J., Burke, M. S., Batchellor, A. S. & Boettcher, S. W. Effects of intentionally incorporated metal cations on the oxygen evolution electrocatalytic activity of nickel (oxy)hydroxide in alkaline media. *ACS Catal.* **6**, 2416–2423 (2016).
4. Grimaud, A. et al. Activating lattice oxygen redox reactions in metal oxides to catalyse oxygen evolution. *Nat. Chem.* **9**, 457–465 (2017).
5. Man, I. C. et al. Universality in oxygen evolution electrocatalysis on oxide surfaces. *ChemCatChem* **3**, 1159–1165 (2011).
6. Suntivich, J., May, K. J., Gasteiger, H. A., Goodenough, J. B. & Shao-Horn, Y. A perovskite oxide optimized for molecular orbital principles. *Science* **334**, 1383–1385 (2011).
7. Grimaud, A. et al. Double perovskites as a family of highly active catalysts for oxygen evolution in alkaline solution. *Nat. Commun.* **4**, 2439 (2013).
8. Dau, H. et al. The mechanism of water oxidation: from electrolysis via homogeneous to biological catalysis. *ChemCatChem* **2**, 724–761 (2010).
9. Hong, W. T. et al. Toward the rational design of non-precious transition metal oxides for oxygen electrocatalysis. *Energy Environ. Sci.* **8**, 1404–1427 (2015).
10. Umena, Y., Kawakami, K., Shen, J.-R. & Kamiya, N. Crystal structure of oxygen-evolving photosystem II at a resolution of 1.9 Å. *Nature* **473**, 55–60 (2011).
11. Ferreira, K. N., Iverson, T. M., Maghlaoui, K., Barber, J. & Iwata, S. Architecture of the photosynthetic oxygen-evolving center. *Science* **303**, 1831–1838 (2004).
12. Tsui, E. Y. & Agapie, T. Reduction potentials of heterometallic manganese–oxido cubane complexes modulated by redox-inactive metals. *Proc. Natl Acad. Sci. USA* **110**, 10084–10088 (2013).
13. Tsui, E. Y., Tran, R., Yano, J. & Agapie, T. Redox-inactive metals modulate the reduction potential in heterometallic manganese–oxido clusters. *Nat. Chem.* **5**, 293–299 (2013).
14. Kuznetsov, D. A. et al. Tuning redox transitions via inductive effect in metal oxides and complexes, and implications in oxygen electrocatalysis. *Joule* **2**, 225–244 (2018).
15. Xiao, D. J., Oktawiec, J., Milner, P. J. & Long, J. R. Pore environment effects on catalytic cyclohexane oxidation in expanded Fe$_2$(dobdc) analogues. *J. Am. Chem. Soc.* **138**, 14371–14379 (2016).
16. Smith, P. T., Kim, Y., Benke, B. P., Kim, K. & Chang, C. J. Supramolecular tuning enables selective oxygen reduction catalyzed by cobalt porphyrins for direct electrosynthesis of hydrogen peroxide. *Angew. Chem. Int. Ed.* **59**, 4902–4907 (2020).

17. Nguyen, A. I. et al. Manganese–cobalt oxido cubanes relevant to manganese-doped water oxidation catalysts. *J. Am. Chem. Soc.* **139**, 5579–5587 (2017).

18. Jee, A.-Y., Cho, Y.-K., Granick, S. & Tlusty, T. Catalytic enzymes are active matter. *Proc. Natl Acad. Sci. USA* **115**, E10812–E10821 (2018).

19. Mozhaev, V. V. in *Stability and Stabilization of Biocatalysts* (ed. Ballesteros, A.) 355–363 (Elsevier Science, 1998).

20. Kalmutzki, M. J., Hanikel, N. & Yaghi, O. M. Secondary building units as the turning point in the development of the reticular chemistry of MOFs. *Sci. Adv.* **4**, eaat9180 (2018).

21. Jiao, L., Wang, Y., Jiang, H.-L. & Xu, Q. Metal–organic frameworks as platforms for catalytic applications. *Adv. Mater.* **30**, 1703663 (2018).

22. Pullen, S., Fei, H., Orthaber, A., Cohen, S. M. & Ott, S. Enhanced photochemical hydrogen production by a molecular diiron catalyst incorporated into a metal–organic framework. *J. Am. Chem. Soc.* **135**, 16997–17003 (2013).

23. Jahan, M., Bao, Q. & Loh, K. P. Electrocatalytically active graphene–porphyrin MOF composite for oxygen reduction reaction. *J. Am. Chem. Soc.* **134**, 6707–6713 (2012).

24. Kornienko, N. et al. Metal–organic frameworks for electrocatalytic reduction of carbon dioxide. *J. Am. Chem. Soc.* **137**, 14129–14135 (2015).

25. Nguyen, A. I. et al. Stabilization of reactive Co_4O_4 cubane oxygen-evolution catalysts within porous frameworks. *Proc. Natl Acad. Sci. USA* **116**, 11630–11639 (2019).

26. Huang, Z.-L. et al. Ab-initio XPRD crystal structure and giant hysteretic effect (H_c = 5.9 T) of a new hybrid terephthalate-based cobalt(II) magnet. *Chem. Mater.* **12**, 2805–2812 (2000).

27. Zhao, S. et al. Ultrathin metal–organic framework nanosheets for electrocatalytic oxygen evolution. *Nat. Energy* **1**, 16184 (2016).

28. Li, W. et al. Unprecedented high oxygen evolution activity of electrocatalysts derived from surface-mounted metal–organic frameworks. *J. Am. Chem. Soc.* **141**, 5926–5933 (2019).

29. Zhao, S. et al. Structural transformation of highly active metal–organic framework electrocatalysts during the oxygen evolution reaction. *Nat. Energy* **5**, 881–890 (2020).

30. Zheng, W. & Lee, L. Y. S. Metal–organic frameworks for electrocatalysis: catalyst or precatalyst? *ACS Energy Lett.* **6**, 2838–2843 (2021).

31. Bonnet, S. et al. Synthesis of hybrid organo–mineral materials: anionic tetraphenylporphyrins in layered double hydroxides. *Chem. Mater.* **8**, 1962–1968 (1996).

32. Leroux, F. et al. Delamination and restacking of layered double hydroxides. *J. Mater. Chem.* **11**, 105–112 (2001).

33. Islam, M. & Patel, R. *Organic–Inorganic Hybrid Ion-Exchangers and Layered Double Hydroxides: Synthesis, Characterization and Environmental Application* (Lambert Academic Publishing, 2009).

34. Burtch, N. C., Jasuja, H. & Walton, K. S. Water stability and adsorption in metal–organic frameworks. *Chem. Rev.* **114**, 10575–10612 (2014).

35. Greczynski, G. & Hultman, L. X-ray photoelectron spectroscopy: towards reliable binding energy referencing. *Prog. Mater. Sci.* **107**, 100591 (2020).

36. Wang, Y., Yan, D., El Hankari, S., Zou, Y. & Wang, S. Recent progress on layered double hydroxides and their derivatives for electrocatalytic water splitting. *Adv. Sci.* **5**, 1800064 (2018).

37. Dean, J. A. *Lange's Handbook of Chemistry* (McGraw-Hill, 1999).

38. Bockris, J., Reddy, A. & Gamboa-Aldeco, M. in *Modern Electrochemistry, 2A: Fundamentals of Electrodics* 1175–1187 (Springer, 2000).

39. Rao, R. R. et al. Operando identification of site-dependent water oxidation activity on ruthenium dioxide single-crystal surfaces. *Nat. Catal.* **3**, 516–525 (2020).

40. Friebel, D. et al. Identification of highly active Fe sites in (Ni,Fe)OOH for electrocatalytic water splitting. *J. Am. Chem. Soc.* **137**, 1305–1313 (2015).

41. Diaz-Morales, O., Ferrus-Suspedra, D. & Koper, M. T. M. The importance of nickel oxyhydroxide deprotonation on its activity towards electrochemical water oxidation. *Chem. Sci.* **7**, 2639–2645 (2016).

42. Xiao, H., Shin, H. & Goddard, W. A. Synergy between Fe and Ni in the optimal performance of (Ni,Fe)OOH catalysts for the oxygen evolution reaction. *Proc. Natl Acad. Sci. USA* **115**, 5872–5877 (2018).

43. Dionigi, F. et al. In-situ structure and catalytic mechanism of NiFe and CoFe layered double hydroxides during oxygen evolution. *Nat. Commun.* **11**, 2522 (2020).

44. Hu, C. et al. Surface-enhanced Raman spectroscopic evidence of key intermediate species and role of NiFe dual-catalytic center in water oxidation. *Angew. Chem. Int. Ed.* **60**, 19774–19778 (2021).

45. Giordano, L. et al. pH dependence of OER activity of oxides: current and future perspectives. *Catal. Today* **262**, 2–10 (2016).

46. Gorlin, M. et al. Tracking catalyst redox states and reaction dynamics in Ni–Fe oxyhydroxide oxygen evolution reaction electrocatalysts: the role of catalyst support and electrolyte pH. *J. Am. Chem. Soc.* **139**, 2070–2082 (2017).

47. Kuznetsov, D. A., Peng, J., Giordano, L., Román-Leshkov, Y. & Shao-Horn, Y. Bismuth substituted strontium cobalt perovskites for catalyzing oxygen evolution. *J. Phys. Chem. C* **124**, 6562–6570 (2020).

48. Lee, Y., Suntivich, J., May, K. J., Perry, E. E. & Shao-Horn, Y. Synthesis and activities of rutile IrO_2 and RuO_2 nanoparticles for oxygen evolution in acid and alkaline solutions. *J. Phys. Chem. Lett.* **3**, 399–404 (2012).

49. Kuai, C. et al. Fully oxidized Ni–Fe layered double hydroxide with 100% exposed active sites for catalyzing oxygen evolution reaction. *ACS Catal.* **9**, 6027–6032 (2019).

50. Stoerzinger, K. A., Qiao, L., Biegalski, M. D. & Shao-Horn, Y. Orientation-dependent oxygen evolution activities of rutile IrO_2 and RuO_2. *J. Phys. Chem. Lett.* **5**, 1636–1641 (2014).

Methods

Materials and instrumentation. All reagents and solvents were commercially available and used as received. The H$_2$L1 (terephthalic acid), H$_2$L2 (2,6-naphthalene dicarboxylic acid) and H$_2$L3 (4,4′-biphenyl dicarboxylic acid) were purchased from Sigma-Aldrich, while H$_2$L4 (azobenzene-4,4′-dicarboxylic acid) and H$_2$L4F (2,2′-difluoroazobenzene-4,4′-dicarboxylic acid) were synthesized using a method reported in the literature[51] with modifications (details in the Supplementary Information). Gas sorption measurements were conducted using a Micromeritics ASAP 2020 system. Powder X-ray diffraction was carried out with a Bruker D8-Focus Bragg-Brentano X-ray powder diffractometer equipped with a Cu-sealed tube (wavelength, $\lambda = 1.5418$ Å) at 40 kV and 40 mA. Ultraviolet–visible (UV–vis) absorption spectra were recorded on a Cary 5000 UV–Vis–NIR spectrophotometer. Thermogravimetric analysis was conducted on a TA Instruments Q500 thermogravimetric analyser. Inductively coupled plasma optical emission spectroscopy data were collected with an Agilent 5100 DVD inductively coupled plasma optical emission spectrometer. Atomic force microscopy data were collected with a Dimension 3000 scanning probe microscope. TEM experiments were conducted on a JEOL JEM2100 microscope at 200 kV, where images were recorded using a Gatan Orius 833 CCD (charge-coupled device) camera under low-dose conditions. HR-TEM experiments were performed on a FEI Tecnai G2 F30 microscope at an accelerating voltage of 300 kV and an image-spherical-aberration-corrected FEI Titan 80-300 microscope at 300 kV. High-angle annular dark-field scanning transmission electron microscopy imaging and energy-dispersive X-ray mapping were conducted with a Talos F200X microscope equipped with a Super-X EDXS detector system (FEI) at 200 kV. Scanning electron microscopy images were collected on a FEI Quanta 600 field emission scanning electron microscope (America) at 20 kV, where 10 nm platinum/palladium films were sputtered on samples before the measurements. XPS was performed with a Thermo Scientific K-Alpha ESCA spectrometer using monochromatic Al K$_\alpha$ radiation (1,486.6 eV) and a low-energy flood gun as a neutralizer, and the binding energy of the C 1s peak at 284.6 eV was used as a reference. More details are provided in the Supplementary Information.

Synthesis of bulk MHOFs. Generally, bulk MHOFs were prepared by the reaction between M(OH)$_2$ and a carboxylate linker under solvothermal conditions at 120 °C. Taking Ni$_2$(OH)$_2$(L4) as an example, freshly prepared Ni(OH)$_2$ precursor (50 mg, 0.54 mmol), H$_2$L4 (70 mg, 0.26 mmol), N,N-dimethylformamide (DMF; 16 ml), water (1 ml) and ethanol (1 ml) were charged into a Pyrex vial. The mixture was heated at 120 °C for 12 h. After cooling to room temperature, the product was collected by centrifugation, washed with DMF (two times) and acetone (two times) and dried at 100 °C under vacuum (95 mg, 87 at.% yield). More details are provided in the Supplementary Information.

Synthesis of Ni$_2$(OH)$_2$(L4) nanosheets. The NiCl$_2$·6H$_2$O (100 mg, 0.42 mmol), H$_2$L4 (100 mg, 0.37 mmol), DMF (16 ml), water (1 ml) and ethanol (1 ml) were charged into a Pyrex vial. The mixture was heated at 120 °C for 12 h. After cooling to room temperature, the product was collected by centrifugation, dispersed in ethanol, sonicated for 30 min and dried at 100 °C under vacuum (75 mg, 85 at.% yield).

Synthesis of M/Ni$_2$(OH)$_2$(L4) nanosheets. Generally, metal-substituted MHOF nanosheets were prepared by the reaction between NiCl$_2$·6H$_2$O, H$_2$L4 and respective heterometal salts under solvothermal conditions at 120 °C. Taking Fe/Ni$_2$(OH)$_2$(L4) as an example, NiCl$_2$·6H$_2$O (90 mg, 0.38 mmol), FeCl$_2$·4H$_2$O (10 mg, 0.05 mmol), H$_2$L4 (100 mg, 0.37 mmol), DMF (16 ml), water (1 ml) and ethanol (1 ml) were charged into a Pyrex vial. The mixture was heated at 120 °C for 12 h. After cooling to room temperature, the product was collected by centrifugation, dispersed in ethanol, sonicated for 30 min and dried at 100 °C under vacuum (70 mg, 78 at.% yield). The Fe/(Ni + Fe) ratio was determined to be 12.5 at.% by inductively coupled plasma optical emission spectroscopy.

Electrochemical measurements of OER activities. Electrodes for CV and galvanostatic measurements were prepared by drop-casting an ink containing oxide catalyst powder on a glassy carbon electrode. Typically, the ink contained 5 mg MHOFs, 2 ml water/ethanol (2:3) and 0.01 ml 5 wt% Nafion solution. The glassy carbon electrode surface (0.196 cm^2) was loaded with 125 μg cm$^{-2}_{geo.}$ of the catalyst and 20 μg cm$^{-2}_{geo.}$ of Nafion, while an additional 25 μg cm$^{-2}_{geo.}$ of acid-treated acetylene carbon black was used for Fe/Ni$_2$(OH)$_2$(L4)/C. Electrochemical measurements were performed using a glass electrochemical cell with Ag/AgCl reference electrode and Pt counter electrode in a rotating disk electrode set-up in Ar- or O$_2$-saturated KOH (99.99% purity, Sigma-Aldrich) electrolytes. The Ag/AgCl reference electrode was calibrated in the same electrolyte by measuring the hydrogen oxidation/evolution using a platinum working electrode and defining the point of zero current as 0 V$_{RHE}$. The potential was controlled using a Biologic VSP-300 potentiostat. CV measurements were performed at a scan rate of 10 mV s^{-1}, while galvanostatic measurements were performed at different current densities at a rotation speed of 1,600 r.p.m. Ohmic losses were corrected by subtracting the ohmic drop from the measured potential using an electrolyte resistance determined by high-frequency alternating current impedance, where iR-corrected potentials are denoted as $E - iR$ (with i as the current and R as the electrolyte resistance). More details are provided in the Supplementary Information.

Data availability

The X-ray crystallographic data for structures reported in this article have been deposited at the Cambridge Crystallographic Data Centre (CCDC) under deposition numbers CCDC 2120871, 2120868, 2120869 and 2120870 for Ni$_2$(OH)$_2$(L1), Ni$_2$(OH)$_2$(L2), Ni$_2$(OH)$_2$(L3) and Ni$_2$(OH)$_2$(L4), respectively, which can be obtained from the CCDC via https://www.ccdc.cam.ac.uk/structures/. All other data that support the results in this study are available from the corresponding authors upon reasonable request.

References

51. Mukherjee, P. S., Das, N., Kryschenko, Y. K., Arif, A. M. & Stang, P. J. Design, synthesis, and crystallographic studies of neutral platinum-based macrocycles formed via self-assembly. *J. Am. Chem. Soc.* **126**, 2464–2473 (2004).

Author contributions

Y.S.-H., Y.R.-L., S.Y. and B.C. conceived the original idea. S.Y. performed the synthesis. S.Y., J.P. and B.C. performed the electrochemical measurements and data analysis. J.P. and L.G. conducted the DFT calculations. Z.H., R.H. and X.Z. performed the TEM analysis. A.T.G.-E. and D.S. conducted the X-ray absorption spectroscopy measurements and data analysis. J.P., Y.Z., K.A. and Y.G.Z. performed the XPS, diffuse reflectance infrared Fourier transform spectra, inductively coupled plasma optical emission spectroscopy and scanning electron microscopy measurements. S.Y., J.P., B.C., Y.S.-H. and Y.R.-L. draughted the manuscript. All authors contributed to the revision of the manuscript.

Competing interests

The authors declare no competing interests.

Additional information

Supplementary information The online version contains supplementary material available at https://doi.org/10.1038/s41563-022-01199-0.

Correspondence and requests for materials should be addressed to Yuriy Román-Leshkov or Yang Shao-Horn.

Peer review information *Nature Materials* thanks the anonymous reviewers for their contribution to the peer review of this work.

Reprints and permissions information is available at www.nature.com/reprints.